

DOPAMINE: Doppler frequency and Angle of arrival MINimization of tracking Error for extended reality

Andrea Bedin

Nokia Bell Labs

Espoo, Finland

University of Padova, DEI

Padova, Italy

andrea.bedin.2@studenti.unipd.it

Alexander Marinšek

KU Leuven, ESAT-WaveCore

9000 Ghent, Belgium

alexander.marinsek@kuleuven.be

Shaghayegh Shahcheraghi

Technical University of Darmstadt

Darmstadt, Germany

sshahcheraghi@wise.tu-darmstadt.de

Nairy Moghadas Gholian

Technical University of Darmstadt

Darmstadt, Germany

ngholian@wise.tu-darmstadt.de

Liesbet Van der Perre

KU Leuven, ESAT-WaveCore

9000 Ghent, Belgium

liesbet.vanderperre@kuleuven.be

ABSTRACT

In this paper, we investigate how Joint Communication And Sensing (JCAS) can be used to improve the Inertial Measurement Unit (IMU)-based tracking accuracy of eXtended Reality (XR) Head-Mounted Displays (HMDs). Such tracking is used when optical and InfraRed (IR) tracking is lost, and its lack of accuracy can lead to disruption of the user experience. In particular, we analyze the impact of using doppler-based speed estimation to aid the accelerometer-based position estimation, and Angle of Arrival (AoA) estimation to aid the gyroscope-based orientation estimation. Although less accurate than IMUs for short times in fact, the JCAS based methods require one fewer integration step, making the tracking more sustainable over time. Based on the proposed model, we conclude that at least in the case of the position estimate, introducing JCAS can make long lasting optical/IR tracking losses more sustainable.

CCS CONCEPTS

• Human-centered computing → *Displays and imagers*; • Hardware → *Digital signal processing*; *Wireless devices*; *Wireless integrated network sensors*; Sensor devices and platforms.

KEYWORDS

Extended reality, Joint Communication and Sensing, mmWave

1 INTRODUCTION

Accurately tracking the position of eXtended Reality (XR) Head-Mounted Displays (HMDs) is critical for maintaining high user Quality of Experience (QoE). Modern HMDs achieve this using precise visible/InfraRed (IR) light tracking equipment. Unfortunately, visual/IR tracking is also prone to outage in adverse circumstances.

Permission to make digital or hard copies of all or part of this work for personal or classroom use is granted without fee provided that copies are not made or distributed for profit or commercial advantage and that copies bear this notice and the full citation on the first page. Copyrights for components of this work owned by others than ACM must be honored. Abstracting with credit is permitted. To copy otherwise, or republish, to post on servers or to redistribute to lists, requires prior specific permission and/or a fee. Request permissions from permissions@acm.org.

Emerging Wireless '22, December 9, 2022, Roma, Italy

© 2022 Association for Computing Machinery.

ACM ISBN 978-1-4503-9934-0/22/12...\$15.00

<https://doi.org/10.1145/3565474.3569072>

Although an HMD can switch to Inertial Measurement Unit (IMU) based tracking in such situations, long term visual/IR outage will result in error buildup due to accelerometer and gyroscope drift integration. HMDs mostly rely on two major visual/IR tracking techniques: a) the HMD gathers visual/IR information from an illuminated environment or b) the HMD receives visual/IR signals from multiple external beacons in its vicinity. Examples of HMDs fitted with a) and b) tracking options are the Oculus Quest 2 and the HTC Vive 2, respectively. Option a) is inherently prone to accuracy variations and outage due to limited control over environment illumination. Option b) offers precise tracking when the beacons lie within the HMD's field of view; yet, it experiences outage as soon as the HMD loses sight of the external beacons [7]. A possible cause is either the user waving their hand or another object passing between a beacon and the HMD. Moreover, the XR users can rotate their head away from the IR light sources. Outage can befall HMDs equipped with option a) tracking in a similar manner when the main light source is blocked. Hence, manufacturers should foresee visual/IR tracking outage and provide the HMD with alternative tracking solutions. To avoid error-prone HMD-based tracking during longer visual/IR tracking outage, the wireless communication transceivers in an HMD can double as a sensing device. The transceiver provides directly the HMD orientation through Angle of Arrival (AoA) estimation, while velocity is extracted from Doppler frequency shift estimation; thus, removing the need for one numerical integration step in both cases, compared to IMU tracking. Sensing the environment by estimating the AoA, Time of Arrival (ToA), or Doppler frequency extracted from communication signals, called Joint Communication and Sensing (JCAS) has been proposed used in recent literature [1, 4–6]. In the work at hand, we propose and evaluate a **Dopamine** technique for **minimizing** XR HMD tracking error during visual/IR tracking outage, called Dopamine. The proposed approach can be used alongside IMU-based tracking and substitute it dynamically upon error accumulation. Dopamine is primarily designed to operate in the 60 GHz millimeter wave (mmWave) frequency band and loosely conform with conventions standardized in IEEE 802.11ad/ay. Moreover, Dopamine's flexibility allows for easy portability to other frequency bands and standards. Our contributions are three-fold: I)

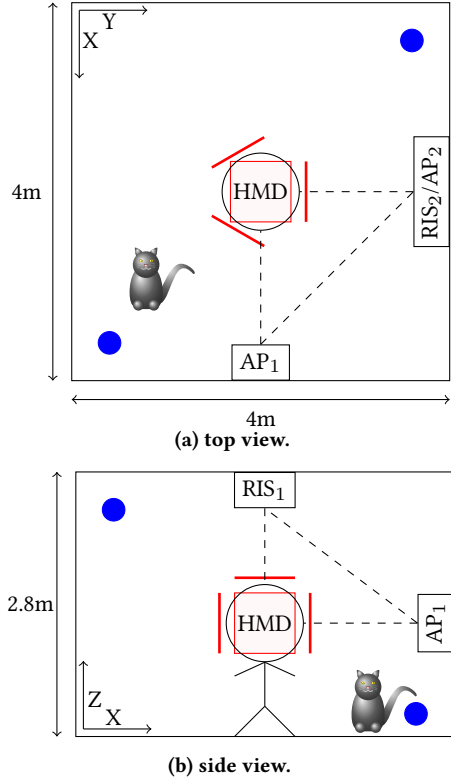


Figure 1: Considered scenario. Dashed black lines represent signal propagation paths between the APs, RISs, and the HMD. UPAs are marked in red, while the two IR light tracking beacons are depicted in blue and the blocker is depicted in gray.

the extraction of HMD tracking data using limited wireless channel information, II) the analysis of tracking performance when employing either multiple Access Points or multiple Reconfigurable Intelligent Surfaces, and III) the evaluation of the proposed tracking technique against IMU-based tracking.

The paper is structured as follows: Section 2 defines a simple scenario that will be used for the evaluation, Section 3 describes the Dopamine tracking and estimation framework, Section 4 presents and discusses the performance results, while Section 5 draws a conclusion on the study's findings and highlights future research areas.

2 SYSTEM MODEL

The following subsections describe the considered scenario, including the environment description, wireless signal propagation modeling, and an overview of XR user mobility. Table 1 lists the most relevant system parameters.

2.1 Environment

Figure 1 depicts the considered environment. Although it is very specific, we consider it is representative of a realistic XR scenario and the results obtained will be indicative of the potential improvement in tracking brought by the method. An XR user is positioned

in the middle of a square room with a 2.8 m high ceiling and measuring 4 m in length and width. The main AP (AP₁) is placed on the southern wall at a height of 1.8 m, while the main RIS (RIS₁) is attached to the ceiling, directly above the user. Either a second AP or RIS (AP₂/RIS₂) is placed on the eastern wall at the same height as AP₁. The use of RISs is essential to ensure that the system has a reasonable cost: mmWave APs are very costly, and multi-AP solutions might not become available in the near future.

The HMD is equipped with 4 square Uniform Planar Arrays (UPAs). One is attached to the top headband of the HMD, orienting it directly towards RIS₁. The remaining 3 are spread out along the HMD's frame and horizontal headband, misaligned by 120°. This provides full azimuth coverage since the considered microstrip antennas with 5 dBi directivity have a 120° half-power beam width (HPBW) [12]. Thus, the HMD receiver design features 4 RF chains, one for each UPA, of which only 3 are employed for tracking purposes at any one time. Compared to a fully digital MIMO system, this is more feasible in resource-constrained consumer devices, which we assume will anyway feature multiple phased antenna arrays for coping with mobility and adverse circumstances.

Two additional IR light tracking beacons are foreseen in the room to highlight the problem at hand. The beacons are placed in two corners of the room, and we assume one is covered by an obstructing object. The wireless data link can serve as a supportive tracking technology as long as the visual/IR beacons and the APs/RISs are not co-located.

2.2 Wireless signal propagation

Determining the received signal strength at the HMD P_{RX} is the basis for evaluating Dopamine's performance as an RF-tracking alternative. Without further denoting the dependency on system parameters for now, the received signal strength is derived as follows:

$$P_{RX} = P_{TX} + G_{RX} + G_{RIS} - PL \quad (1)$$

where P_{TX} is the transmitted signal power – set to 24 dBm as in TP-Link Talon AD7200 APs [10] – G_{RX} and G_{RIS} are the ensemble Receiver (RX) and RIS power gain, respectively, while PL corresponds to signal attenuation due to path loss.

RX power gain is governed by antenna element directivity and array gain. The 120° HPBW antenna radiation patterns are modeled as a cosine of the azimuth angle [3], while the number of antenna elements contributes to the array gain according to:

$$G_{RX}(\varphi, M) = \underbrace{10 \log_{10}(\pi \cos(\varphi))}_{\text{antenna gain}} + \underbrace{10 \log_{10}(MN)}_{\text{array gain}} \quad (2)$$

where φ is the impinging wave's azimuth angle and $M = N = 4$ represents the number of array elements, in the vertical and horizontal direction. We consider the worst case azimuth misalignment ±60° for the three UPAs in the horizontal plane in all further calculations. This may happen while the XR user is rotating. The misalignment reduces antenna gain to 2 dBi, yielding a 14 dB receive gain. Contrarily, the UPA on the top headband has boresight conditions to RIS₁, resulting in 17 dB gain. We apply the RIS power radiation pattern from [9] in both receive and transmit direction due to reciprocity. We assume the RISs are sufficiently small (e.g.

Table 1: System parameters.

Name	Value	Name	Value
Room dimensions	4x4x2.8 m	HMD / AP / RIS height	1.8 m
AP ₁ -RIS ₂ / distance	2.8 m	AP ₁ / AP ₂ / RIS ₁ -HMD distance	2 m
Carrier frequency (f_0)	60 GHz	Transmit power (P_{TX})	24 dBm
Thermal noise power	-82 dBm	Noise figure	10 dB
Receive gain (G_{RX})	14–17 dB	HMD antenna HPBW	120°
HMD antenna arrays	4	HMD array size ($M \times N$)	4x4
RIS gain (G_{RIS})	0 dB	x	x
HMD display refresh rate	120 Hz	PHY packet rate (R_p)	50 Kpkt/s
Movement bandwidth (B_m)	30 Hz	Beam training interval (T_b)	102.4ms

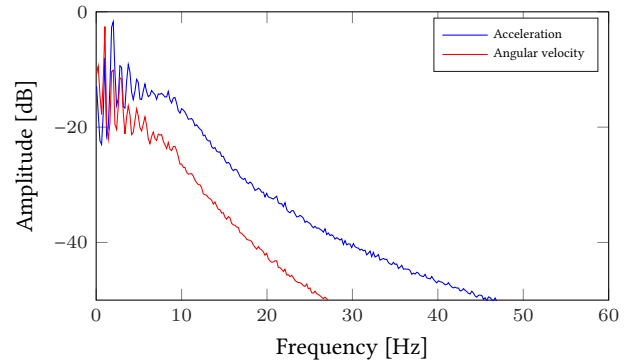
Table 2: Worst-case SNR for each scenario.

Path	SNR [dB]
AP ₁ -HMD or AP ₂ -HMD	36
AP ₁ -RIS ₁ -HMD	36
AP ₁ -RIS ₂ -HMD	28

a 5x5 cm panel with 10x10 elements), resulting in a far-field distance less than 1 m. The ceiling-mounted RIS₁ is oriented so that it's 0-elevation plane crosses through both the HMD and AP₁, giving it unitary gain. Similarly, $G_{RIS} = 0$ dB applies to RIS₂ if its 0-elevation plane is level to the ground. Attenuation due to the propagation distance is modelled according to the free-space path loss equation: $PL = 20 \log_{10} \left(\frac{4\pi d}{\lambda} \right)$, where d represents the total length of the propagation path and λ is the 5 mm wavelength at 60 GHz. Finally, we use the derived receive power P_{RX} to calculate the Signal to Noise Ratio (SNR): $SNR = P_{RX} - P_N - NF$, where P_N corresponds to thermal noise at room temperature (300 K) for the IEEE 802.11ad/ay 1.76 GHz channel bandwidth (without guard frequencies) and NF stands for an additional 10 dB noise figure [2]. Table 2 lists the derived SNR values for each of the considered propagation paths. Note, that the first two values are equal since the 3 dB loss due to user yaw misalignment (60°) is identical to the added path loss in AP₁-RIS₁-HMD. Beam training sequences (e.g. BRP) can be appended to PHY packets with minimal overhead in case of low gain when beaming in multiple directions, i.e. towards RIS₁ and RIS₂.

2.3 XR user mobility overview

Understanding the characteristics of the user's mobility is necessary to properly design a tracking system. For this purpose, we used the dataset from [11] to determine the frequency content of the movements. In particular, we selected all the files reporting acceleration data and gyroscope data, estimated the Power Spectral Density (PSD) of the signal using Welch's algorithm for each file and averaged all the PSDs over all files. In the result, shown in figure 2, we observe that for frequency over $B_m = 30$ Hz the normalized PSD has negligible amplitude. For this reason, we require the sensors to be sampled more than 30 times per second. Moreover, we also evaluated the Root Mean Square (RMS) and maximum value for

**Figure 2: Normalized spectrum of the acceleration and angular velocity.**

the acceleration and angular velocity thought the whole dataset. The resulting values are of 38°/s and 261°/s for the gyroscope and 1.8 $\frac{m}{s^2}$ and 14 $\frac{m}{s^2}$ for the accelerometer.

3 ESTIMATION

In this section, we describe how the position and rotation of the headset can be tracked using Joint Communication And Sensing (JCAS), and compare the radio-based tracking with the IMU-based tracking.

3.1 MUSIC

In this paper, we use MUltiple SIgnal Classification (MUSIC) to perform spectral and AoA estimations. MUSIC is a subspace-based high resolution algorithm which divides the received signal space into two subspaces, called the signal subspace and the noise subspace. It relies on the eigenvalue decomposition of the covariance matrix of the received signal, $R_y = E[\mathbf{y}\mathbf{y}^H]$, where \mathbf{y} is the signal of interest impaired by noise. MUSIC computes all the eigenvalues and their associated eigenvectors of R_y , and it splits the eigenvalues into two categories based on their magnitude. It considers the eigenvectors corresponding to the "large" eigenvalues as the vectors that span the signal subspace and the eigenvectors corresponding to the "near-zero" eigenvalues to span the Noise-subspace. The latter are the columns of the so-called noise matrix U_n . The estimated frequency or AoA of the incident signals are the peaks of MUSIC

spectrum $P_{MUSIC}(X) = \frac{1}{a^H(X)U_nU_n^H a(X)}$, where U_n is the noise matrix, and $a(X)$ is the steering vector associated with X , and X is either a frequency, in case of spectral estimation, a pair of angles in case of 2D AoA estimation or a single angle in case of 1D AoA estimation.

3.2 Velocity

The velocity of the headset can be estimated based on the doppler effect measured on the received signal. This choice is mainly driven by the characteristics of 802.11ad/ay: as the Doppler frequency is proportional to the carrier frequency, mmWave systems can be very sensitive to movements provide very accurate velocity estimation. In particular, for the k -th received packet we assume to obtain a Channel Frequency Response (CFR) estimate from a beam pointing in the x , y and z direction, and that the received signal is dominated by the Line of Sight (LoS) to the AP₁, AP₂/RIS₂ and RIS₁ respectively. In the following, we only consider the movement in the x direction, as the other directions can be modelled in the same way. We also assume that the initial position of the device is at 0, i.e. at the beginning of the outage the receiver is perfectly synchronized (i.e. at time 0 the frequency response is constant). With this assumption, the channel CFR can be written as

$$H(k, f) = \alpha e^{-\frac{j2\pi(f_0+f)\sum_{i=0}^K v_x(i)}{cR_p}} \quad (3)$$

Where α is assumed to be a constant channel coefficient and $v_x(i)$ is the velocity of the headset along the x direction. In order to observe the effect of movement, we assume to observe the channel K times. If the speed and orientation are constant throughout the observation, i.e. $v_x(i) = v_x$ for some constant v_x , and using the approximation $(f_0 + f) \approx f_0$, since $f \ll f_0$, we can approximate the channel to:

$$H(k, f) = \alpha e^{-\frac{j2\pi f_0 k v_x}{cR_p}} = \alpha e^{-j2\pi f_d k}. \quad (4)$$

Where $f_d = \frac{f_0 v_x}{cR_p}$ is the frequency of the channel variation over frame. Such frequency can be estimated using the MUSIC algorithm described in section 3.1. The estimated velocity can therefore be computed as $\bar{v}_x = v_x + \mathcal{N}(0, \sigma_{v_x}) = \frac{c f_d R_p}{f_0}$. The observation period length $T = KR_p$ must be designed with the movement characteristics in mind: This value is subject to an inherent trade-off, as a low value gives worse frequency estimates, but for high values the assumption of constant velocity might not be satisfied. In this work, we choose to determine this value empirically by simulating the estimation for different values of T . For each value, we generated 100 channel realizations with an SNR of 30dB, we used a time varying speed $v_x(k) = \frac{k a}{R_p}$, where the acceleration a is a realization of a normal distribution with zero mean and standard deviation $\bar{\sigma}_a$. We repeated the experiment for $\bar{\sigma}_a \in \{0, 10, 20, 40\} \frac{\text{m}}{\text{s}^2}$ and compared the result with the average velocity over the observation $\bar{v} = \frac{1}{K} \sum_{i=0}^{K-1} \frac{i a}{R_p}$. In Figure 3 we can see the Root Mean Square Error (RMSE) of the estimated velocity as a function of the observation time T . Here we can observe how, for the considered values of acceleration and observation period, increasing the observation period always improves the estimate. For this reason, we decide to base the choice of T on the HMD display refresh rate instead, and

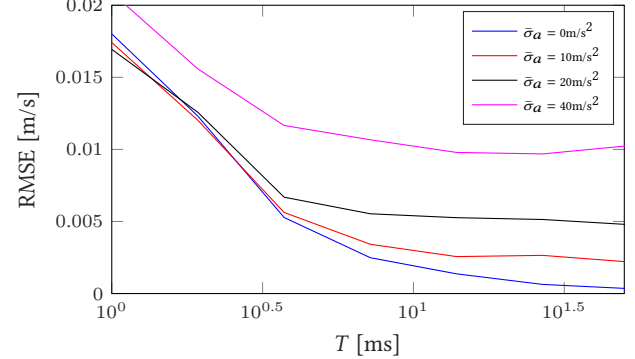


Figure 3: Velocity RMSE vs observation time.

Table 3: Speed RMSE $\sigma_v (\frac{\text{mm}}{\text{s}})$.

Path	profile 1	profile 2
AP ₁ -HMD or AP ₂ -HMD	9.8	3
AP ₁ -RIS ₁ -HMD	9.8	3
AP ₁ -RIS ₂ -HMD	10.9	4.4

use $T = \frac{1}{120\text{Hz}} = 8.3\text{ms}$. Indeed, we can check that this hypothesis leads to a small maximum angle deviation of $261^\circ/\text{s} \cdot T = 2.2^\circ$ over the observation. In order to have a fair comparison, we assume to use the same sampling rate also for the IMU. With these assumptions, the RMSE of the velocity for the three components can be estimated numerically. In order to observe the effect of different movement patterns on the system, we evaluate the error for two acceleration profiles: a) Profile P1: $\bar{\sigma}_a = 10 \frac{\text{m}}{\text{s}^2}$. b) Profile P2: $\bar{\sigma}_a = 40 \frac{\text{m}}{\text{s}^2}$. The corresponding values for each propagation path and profile are listed in table 3.

3.3 Position

We now estimate the velocity for a sequence of L observations. For the ℓ -th observation, calling the noisy estimated velocity $\bar{v}_x^{(\ell)} = v_x^{(\ell)} + \mathcal{N}(0, \sigma_{v_x})$, the position estimate is obtained by integrating the $\bar{v}_x^{(\ell)}$ with respect to ℓ . The positional error is therefore the integral of a white Gaussian noise with a standard deviation of $T\sigma_x$, which results in a standard deviation of the position $\sigma_{p_x}(t) = T\sigma_{v_x} \sqrt{\frac{t}{T}} = (\sqrt{T}\sigma_{v_x})\sqrt{t}$. Assuming uncorrelated errors in the three components of the vector, the expected RMS amplitude of the 3D positional noise is therefore $\|\epsilon_p\|_{\text{RMS}} = \sqrt{(\sigma_{v_x}^2 + \sigma_{v_y}^2 + \sigma_{v_z}^2)Tt}$. By contrast, an accelerometer with an RMS noise of σ_a would result in an acceleration noise process with standard deviation $T\sigma_a$ that, when doubly integrated, leads to an overall positional RMSE of

$$\|\epsilon_p\|_{\text{RMS}} = \sqrt{3 * \left(\frac{T\sigma_a}{\sqrt{3}} \left(\frac{t}{T} \right)^{\frac{3}{2}} \right)^2} = \frac{\sigma_a t^{\frac{3}{2}}}{T} \quad (5)$$

assuming uncorrelated noise in the three components.

3.4 Angle

Unlike speed estimation, the AoA estimation requires full Channel State Information (CSI) for every antenna, so it can only be performed when the beam training is executed. In this paper, we assume that the receiver uses a codebook of 16 orthonormal weights vectors, and call B the unitary matrix that has such vectors as rows. Calling $H_i(f)$ the channel observed by antenna i , we have that the vector of channel $\hat{H}_k(f)$ measured for each beam $k \in [1, 16]$ is

$$\begin{bmatrix} \hat{H}_1(f) \\ \vdots \\ \hat{H}_{16}(f) \end{bmatrix} = B \left(\begin{bmatrix} H_1(f) \\ \vdots \\ H_{16}(f) \end{bmatrix} + \mathcal{N}(0, \sigma I) \right), \quad (6)$$

from which we obtain the noisy estimate of the channel for each antenna

$$\begin{bmatrix} \bar{H}_1(f) \\ \vdots \\ \bar{H}_{16}(f) \end{bmatrix} = B^H \begin{bmatrix} \hat{H}_1(f) \\ \vdots \\ \hat{H}_{16}(f) \end{bmatrix} = \begin{bmatrix} H_1(f) \\ \vdots \\ H_{16}(f) \end{bmatrix} + \mathcal{N}(0, \sigma I). \quad (7)$$

Denoting the elevation and azimuth angle by θ and ϕ respectively, we apply the MUSIC algorithm to the estimated channel for the signal received from AP₁ with steering vector

$$\mathbf{a}(\theta, \phi) = [1, \dots, \Omega^{M-1}, \Phi, \dots, \Omega^{M-1}\Phi, \dots, \Phi^{N-1}, \dots, \Omega^{M-1}\Phi^{N-1}]^T \quad (8)$$

Where $\Omega = e^{-j\pi \sin(\theta) \cos(\phi)}$, $\Phi = e^{-j\pi \sin(\theta) \sin(\phi)}$. For the roll angle γ we use either the signal received from AP₂ or RIS₁ with the steering vector

$$\mathbf{a}(\gamma) = [1, \dots, \Gamma^{M-1}, 1, \dots, \Gamma^{M-1}, \dots, 1, \dots, \Gamma^{M-1}]^T \quad (9)$$

where $\Gamma = e^{-j\pi \sin(\gamma)}$. In our environment, the two possible propagation paths that can be used for roll estimation have the same attenuation. We therefore do not specify which one is used. The RMSE of the orientation is evaluated numerically through simulation and turns out to be $\sigma_0 = 0.4421$.

As the beam training interval $T_b = 102.4$ ms (e.g. one beacon interval in 802.11ad/ay) is large, and therefore the angle update rate $\frac{1}{T_b} \approx 9.8\text{Hz} < B_m$ is lower than the movement bandwidth, we cannot directly use the AoA estimate to determine the orientation. For this reason, we propose to re-calibrate the angle obtained by the gyroscope at every beam training. If we assume that the first beam training happens at time 0, the gyroscope has an RMSE error of σ_g and the error is identical and independent for all components, the uncertainty in the angle can be computed as¹

$$\|\epsilon_a\|_{\text{RMS}}(t) = \sum_{k=0}^{\infty} \sqrt{\sigma_0^2 + 3\sigma_g^2 T(t - kT_b)} u([kT_b, (k+1)T_b]), \quad (10)$$

Whereas the uncertainty for the gyroscope is simply $\|\epsilon_a\|_{\text{RMS}}(t) = (\sqrt{3T}\sigma_g)\sqrt{t}$. Notably, the expression in equation (10) is bounded in the interval $[\sigma_0, \sqrt{\sigma_0^2 + 3\sigma_g^2 T T_b}]$ for any t .

¹ $u([a, b])$ is the characteristic function of the interval $[a, b]$

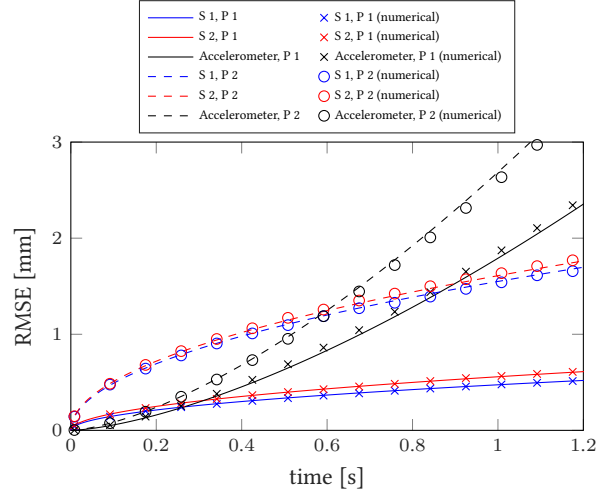


Figure 4: Positional error vs time.

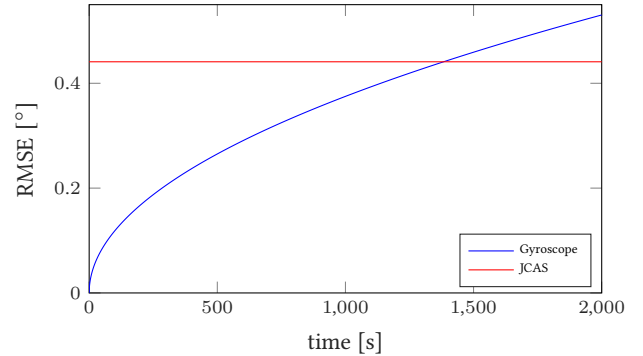


Figure 5: Angular error vs time.

4 RESULTS

In this section, we compare the position and orientation estimates obtained from the JCAS method and the IMU. We consider two different propagation scenarios: (1) Scenario S1: 2 AP and 1 RIS. AP₁ is used for the x velocity component, as well as for azimuth and elevation, AP₂ for the y velocity component and roll, and RIS₁ for the z velocity component. (2) Scenario S2: 1 AP and 2 RISs. AP₁ is used for the x velocity component, as well as for azimuth and elevation, RIS₂ for the y velocity component and roll, and RIS₁ for the z velocity component. As a typical off the shelf IMU, we use the device described in [8], and we assume that the accelerometer is configured to the 4G and 16G acceleration ranges for the acceleration profiles P1 and P2 y. With this assumption, the noise variance σ_a is 2 mg for P1 and 3 mg for P2. Figure 4 shows how the RMS of the position error of the JCAS and accelerometer evolves over time. In the plot, we can see how after around 0.25 seconds for profile P1 and 0.6 seconds for profile P2, the JCAS positional estimate outperforms the accelerometer. Moreover, we also validated the theoretical formulation by numerically integrating 1000 realizations of the white noise evaluating the RMSE. As it can be seen in the plot, the theoretical RMSE matches with the numerical results.

In figure 5 we show how the angular error evolves over time. In this case, the JCAS solution outperforms the IMU only after roughly 20 minutes, making its application impractical.

5 CONCLUSION

In this paper we show that, with the proposed scenario and model, integrating JCAS-based speed estimation can significantly improve HMD tracking when visual/IR tracking outage occurs. In particular, thanks to the fewer integration steps required, the estimate provided by the radio is more sustainable over long periods of time. The same can not be said for orientation though, where the classical IMU based tracking still outperforms JCAS for a long period of time. Although the numerical results are not representative of all possible scenarios, the fact that reducing the number of integration steps improves the sustainability of the tracking is. Further investigation, that we leave for future work, is needed to better quantify the gain in a more general setting.

ACKNOWLEDGMENTS

This work has received funding from the European Union's EU Framework Programme for Research and Innovation Horizon 2020 under Grant Agreement No 861222.

REFERENCES

- [1] Sayed Hossein Dokhanchi, Bhavani Shankar Mysore, Kumar Vijay Mishra, and Björn Ottersten. 2019. A mmWave automotive joint radar-communications system. *IEEE Trans. Aerospace Electron. Systems* 55, 3 (2019), 1241–1260.
- [2] IEEE. 2021. *802.11-2020 - IEEE Standard for Information Technology—Telecommunications and Information Exchange between Systems - Local and Metropolitan Area Networks—Specific Requirements - Part 11 Wireless LAN Medium Access Control (MAC) and Physical Layer (PHY) S*. IEEE, S.I. <https://ieeexplore.ieee.org/servlet/opac?punumber=9363691> OCLC: 1244448204.
- [3] ITU. 2018. *Reccomendation ITU-R M.1851-1: Mathematical models for radiodetermination radar systems antenna patterns for use in interference analyses*. ITU, Geneva, Switzerland. <https://www.itu.int/rec/R-REC-M.1851/en>
- [4] Manikanta Kotaru, Kiran Joshi, Dinesh Bharadia, and Sachin Katti. 2015. Spotfi: Decimeter level localization using wifi. In *Proceedings of the 2015 ACM Conference on Special Interest Group on Data Communication*. 269–282.
- [5] Preeti Kumari, Junil Choi, Nuria González-Prelcic, and Robert W Heath. 2017. IEEE 802.11 ad-based radar: An approach to joint vehicular communication-radar system. *IEEE Transactions on Vehicular Technology* 67, 4 (2017), 3012–3027.
- [6] Preeti Kumari, Sergiy A Vorobyov, and Robert W Heath. 2019. Adaptive virtual waveform design for millimeter-wave joint communication-radar. *IEEE Transactions on Signal Processing* 68 (2019), 715–730.
- [7] Diederick C. Niehorster, Li Li, and Markus Lappe. 2017. The Accuracy and Precision of Position and Orientation Tracking in the HTC Vive Virtual Reality System for Scientific Research. *i-Perception* 8, 3 (June 2017), 204166951770820. <https://doi.org/10.1177/204166951770820>
- [8] ST Microelectronics 2019. *LSM6DSO iNEMO inertial module: always-on 3D accelerometer and 3D gyroscope*. ST Microelectronics. Rev. 2.
- [9] Wankai Tang, Ming Zheng Chen, Xiangyu Chen, Jun Yan Dai, Yu Han, Marco Di Renzo, Yong Zeng, Shi Jin, Qiang Cheng, and Tie Jun Cui. 2021. Wireless Communications With Reconfigurable Intelligent Surface: Path Loss Modeling and Experimental Measurement. *IEEE Transactions on Wireless Communications* 20, 1 (2021), 421–439. <https://doi.org/10.1109/TWC.2020.3024887>
- [10] TP-link. 2022. Talon AD7200 specifications. <https://www.tp-link.com/us/home-networking/wifi-router/ad7200/#specifications>. Accessed: 2022-09-01.
- [11] Hang Yan, Qi Shan, and Yasutaka Furukawa. 2017. RIDI: Robust IMU Double Integration. <https://doi.org/10.48550/ARXIV.1712.09004>
- [12] Guangwei Yang, Jian-Ying Li, Dujuan Wei, Shigang Zhou, and Jiangjun Yang. 2018. Broadening the beam-width of microstrip antenna by the induced vertical currents. *IET Microwaves, Antennas & Propagation* 12, 2 (Feb. 2018), 190–194. <https://doi.org/10.1049/iet-map.2017.0295>